PHYSICAL REVIEW D **80,** 124051 (2009)

High accuracy simulations of black hole binaries: Spins anti-aligned with the orbital angular momentum

Tony Chu,[1] Harald P. Pfeiffer,[1,2] and Mark A. Scheel[1]

[1]*Theoretical Astrophysics 350-17, California Institute of Technology, Pasadena, California 91125, USA*

[2]*Canadian Institute for Theoretical Astrophysics, 60 St. George Street, University of Toronto, Toronto, ON M5S 3H8, Canada*

(Received 8 September 2009; published 31 December 2009)

High-accuracy binary black hole simulations are presented for black holes with spins anti-aligned with the orbital angular momentum. The particular case studied represents an equal-mass binary with spins of equal magnitude $S/m^2 = 0.437\,57 \pm 0.000\,01$. The system has initial orbital eccentricity $\sim 4 \times 10^{-5}$, and is evolved through 10.6 orbits plus merger and ringdown. The remnant mass and spin are $M_f = (0.961\,109 \pm 0.000\,003)M$ and $S_f/M_f{}^2 = 0.547\,81 \pm 0.000\,01$, respectively, where M is the mass during early inspiral. The gravitational waveforms have accumulated numerical phase errors of $\lesssim 0.1$ radians without any time or phase shifts, and $\lesssim 0.01$ radians when the waveforms are aligned with suitable time and phase shifts. The waveform is extrapolated to infinity using a procedure accurate to $\lesssim 0.01$ radians in phase, and the extrapolated waveform differs by up to 0.13 radians in phase and about 1% in amplitude from the waveform extracted at finite radius $r = 350M$. The simulations employ different choices for the constraint damping parameters in the wave zone; this greatly reduces the effects of junk radiation, allowing the extraction of a clean gravitational wave signal even very early in the simulation.

DOI: 10.1103/PhysRevD.80.124051 PACS numbers: 04.25.D−, 04.25.dg, 04.30.−w, 04.30.Db

I. INTRODUCTION

Much progress has been made in recent years in the numerical solution of Einstein's equations for the inspiral, merger, and ringdown of binary black hole systems. Since the work of Pretorius [1] and the development of the moving puncture method [2,3], numerical simulations have been used to analyze post-Newtonian approximations [4–19], to investigate the recoil velocity of the final black hole [20–38], and to explore the orbital dynamics of spinning binaries [28,39–43].

Numerical simulations can provide an accurate knowledge of gravitational waveforms, which is needed to make full use of the information obtained from gravitational wave detectors such as LIGO and LISA. Not only can detected gravitational waveforms be compared with numerical results to measure astrophysical properties of the sources of gravitational radiation, but the detection probability itself can be increased via the technique of matched filtering [44], in which noisy data are convolved with numerical templates to enhance the signal.

The production of accurate numerical waveforms is computationally expensive, making it challenging to construct an adequate waveform template bank covering a sufficiently large region of the parameter space of black hole masses and spins. One way of increasing efficiency is to adopt techniques known as spectral methods. For smooth solutions, spatial discretization errors of spectral methods decrease exponentially with increasing numerical resolution. In contrast, errors decrease polynomially for the finite difference methods used in most binary black hole simulations. Not only have spectral methods been used to prepare very accurate initial data [45–59], but they have been used to generate the longest and most accurate binary black hole simulation to date [60].

Following the previous work of [60], this paper presents the first spectral simulation of an orbiting and merging binary with spinning black holes: an equal mass system with spins of the black holes anti-aligned with the orbital angular momentum. Simulations of binaries with spins parallel to the orbital momentum are certainly not new, e.g. [11,28,34,38,39,42,61]. Our goal here is to show that such systems can be simulated with spectral methods, and that the high accuracies achieved for the nonspinning case carry over into this more general regime.

The spin of each black hole is $S/m^2 = 0.437\,57 \pm 0.000\,01$. The determination of this quantity, as well as other spin measures, is explained in more detail in Sec. IV B. The evolution consists of 10.6 orbits of inspiral with an orbital eccentricity of $e \sim 4 \times 10^{-5}$, followed by the merger and ringdown. We find that this simulation has accuracy comparable to that of the simulation presented in [60]. We also present different choices for the constraint damping parameters in the wave zone; these choices cause the initial noise (''junk radiation'') to damp more rapidly, resulting in a useable, almost noise-free waveform much earlier in the simulation.

This paper is organized as follows: In Sec. II, we discuss the construction of our initial data. In Sec. III, we describe the equations, gauge conditions, and numerical methods used to solve Einstein's equations. In Sec. IV, we present several properties of our simulations, including constraints, and the spins and masses of the black holes. In Sec. V, we explain the extraction of gravitational waveforms from the simulation, and the extrapolation of the waveforms to infinity. Finally, in Sec. VI, we discuss outstanding difficulties and directions for future work.

II. INITIAL DATA

The initial data are almost identical to those used in the simulation of an equal-mass, nonspinning black hole binary presented in Refs. [9,60]. We use quasiequilibrium initial data [52,55,62] (see also [48,49]), built using the conformal thin sandwich formalism [63,64], and employing the simplifying choices of conformal flatness and maximal slicing. Quasiequilibrium boundary conditions are imposed on spherical excision boundaries for each black hole, with the lapse boundary condition given by Eq. (33a) of Ref. [55]. The excision spheres are centered at Cartesian coordinates $C_1^i = (d/2, 0, 0)$ and $C_2^i = (-d/2, 0, 0)$, where we choose the same coordinate distance d and the same excision radii as in [9].

Within this formalism, the spin of each black hole is determined by a parameter Ω_r and a conformal Killing vector ξ^i (tangential to the excision sphere); these enter into the boundary condition for the shift β^i at an excision surface [52]. We will use the sign convention of Eq. (40) in Ref. [57], so that positive Ω_r corresponds to corotating black holes. The same value of Ω_r is chosen at both excision surfaces, resulting in black holes with equal spins. In Refs. [9,60], Ω_r was chosen to ensure that the black hole spins vanish [55]. In this paper, we instead fix Ω_r at some negative value, resulting in moderately spinning black holes that counterrotate with the orbital motion.

Two more parameters need to be chosen before initial data can be constructed: The orbital angular frequency Ω_0 and the radial velocity v_r of each black hole. These parameters are determined by an iterative procedure that minimizes the orbital eccentricity during the subsequent evolution of the binary: We start by setting Ω_0 and v_r to their values in the nonspinning evolution of Ref. [65], we solve the initial value equations with a pseudospectral elliptic solver [51], and we evolve for about 1–2 orbits using the techniques described in Sec. III. Analysis of this short evolution yields an estimate for the orbital eccentricity, and improved parameters Ω_0 and v_r that result in a smaller orbital eccentricity. This procedure is identical to Ref. [9], except that we include a term quadratic in t for the function used to fit the radial velocity (ds/dt), to obtain better fits. We repeat this procedure until the eccentricity of the black hole binary is reduced to $e \sim 4 \times 10^{-5}$. Properties of this low-eccentricity initial data set are summarized in the top portion of Table I.

The data in the upper part of Table I are given in units of M_{ID}, the sum of the black hole masses in the initial data. For any black hole (initial data, during the evolution, the remnant black hole after merger), we define its mass using Christodoulou's formula,

$$m^2 = m_{\mathrm{irr}}^2 + \frac{S^2}{4m_{\mathrm{irr}}^2}. \tag{1}$$

We use the apparent horizon area A_{AH} to define the irreducible mass $m_{\mathrm{irr}} = \sqrt{A_{\mathrm{AH}}/(16\pi)}$. The *nonnegative* spin S of each black hole is computed with the spin diagnostics described in [57]. Unless noted otherwise, we compute the spin from an angular momentum surface integral [66,67] using approximate Killing vectors of the apparent horizons, as described in [57,68] (see also [69,70]). We define the dimensionless spin by

TABLE I. Summary of the simulation presented in this paper. The first block lists properties of the initial data, the second block lists properties of the evolution.

Initial Data	
Coordinate Separation	$d/M_{\mathrm{ID}} = 13.354\,418$
Radius of Excision Spheres	$r_{\mathrm{exc}}/M_{\mathrm{ID}} = 0.382\,604$
Orbital Frequency	$\Omega_0 M_{\mathrm{ID}} = 0.018\,786\,2$
Radial Velocity	$v_r = -7.471\,012\,3 \times 10^{-4}$
Orbital Frequency of Horizons	$\Omega_r M_{\mathrm{ID}} = -0.242\,296$
Black Hole Spins	$\chi_{\mathrm{ID}} = 0.437\,85$
ADM Energy	$M_{\mathrm{ADM}}/M_{\mathrm{ID}} = 0.992\,351$
Total Angular Momentum	$J_{\mathrm{ADM}}/M_{\mathrm{ID}}^2 = 0.865\,01$
Initial Proper Separation	$s_0/M_{\mathrm{ID}} = 16.408\,569$
Evolution	
Initial Orbital Eccentricity	$e \approx 4 \times 10^{-5}$
Mass after Relaxation	$M = (1.000\,273 \pm 0.000\,001)M_{\mathrm{ID}}$
Spins after Relaxation	$\chi = 0.437\,57 \pm 0.000\,01$
Time of Merger (Common AH)	$t_{\mathrm{CAH}} = 2399.38\ M$
Final Mass	$M_f = (0.961\,109 \pm 0.000\,003)M$
Final Spin	$\chi_f = 0.547\,81 \pm 0.000\,01$

$$\chi = \frac{S}{m^2}. \tag{2}$$

III. EVOLUTIONS

A. Overview

The Einstein evolution equations are solved with the pseudospectral evolution code described in Ref. [60]. This code evolves a first-order representation [71] of the generalized harmonic system [72–74] and includes terms that damp away small constraint violations [71,74,75]. The computational domain extends from excision boundaries located just inside each apparent horizon to some large radius, and is divided into subdomains with simple shapes (e.g. spherical shells, cubes, and cylinders). No boundary conditions are needed or imposed at the excision boundaries, because all characteristic fields of the system are outgoing (into the black hole) there. The boundary conditions on the outer boundary [71,76,77] are designed to prevent the influx of unphysical constraint violations [78–84] and undesired incoming gravitational radiation [85,86], while allowing the outgoing gravitational radiation to pass freely through the boundary. Interdomain boundary conditions are enforced with a penalty method [87,88].

The gauge freedom in the generalized harmonic formulation of Einstein's equations is fixed via a freely specifiable gauge source function H_a that satisfies the constraint

$$0 = \mathcal{C}_a \equiv \Gamma_{ab}{}^{b} + H_a, \tag{3}$$

where $\Gamma^a{}_{bc}$ are the spacetime Christoffel symbols. We choose H_a differently during the inspiral, plunge, and ringdown, as described in detail in Secs. III C, III D, and III E.

In order to treat moving holes using a fixed grid, we employ multiple coordinate frames [89]: The equations are solved in "inertial frame" that is asymptotically Minkowski, but the grid is fixed in a "comoving frame" in which the black holes do not move. The motion of the holes is accounted for by dynamically adjusting the coordinate mapping between the two frames.[1] This coordinate mapping is chosen differently at different stages of the evolution, as described in Secs. III C, III D, and III E.

The simulations are performed at four different resolutions, N1 to N4. The approximate number of collocation points for these resolutions is given in Table II.

B. Relaxation of Initial Data

The initial data do not precisely correspond to two black holes in equilibrium, e.g., because tidal deformations are not incorporated correctly, and because of the simplifying choice of conformal flatness. Therefore, early in the evolution the system relaxes and settles down into a new steady-state configuration. Figure 1 shows the change in irreducible mass and spin relative to the initial data during the evolution. During the first $\sim 10\ M$ of the evolution, $M_{\rm irr}$ increases by about 3 parts in 10^4 while the spin decreases by about 1 part in 10^4. These changes are resolved by all four numerical resolutions, labeled N1 (lowest) to N4 (highest), and converge with increasing resolution. After the initial relaxation, for $10\ M \lesssim t \lesssim 2350\ M$, the mass is constant to about 1 part in 10^6, as can be seen from the

[1]All coordinate quantities (e.g. trajectories, waveform extraction radii) in this paper are given with respect to the inertial frame unless noted otherwise.

TABLE II. Approximate number of collocation points and CPU usage for the evolutions performed here. The first column indicates the name of the run. $N_{\rm pts}$ is the approximate number of collocation points used to cover the entire computational domain. The three values for $N_{\rm pts}$ are those for the inspiral, plunge, and ringdown portions of the simulation, which are described in Secns. III C, III D, and III E, , respectively. The total run times T are in units of the total Christodoulou mass M [cf. Equation (1)] of the binary.

Run	$N_{\rm pts}$	CPU-h	CPU-h/T
N1	$(64^3, 65^3, 65^3)$	9930	3.4
N2	$(70^3, 72^3, 72^3)$	16 195	5.6
N3	$(76^3, 78^3, 80^3)$	28 017	9.7
N4	$(82^3, 84^3, 87^3)$	44 954	15.5

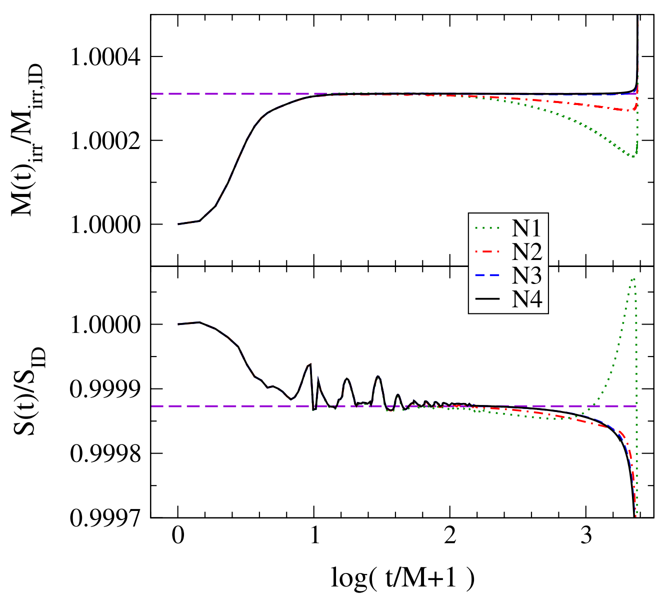

FIG. 1 (color online). Irreducible mass (top panel) and spin (bottom panel) of the black holes during the relaxation of the initial data to the equilibrium (steady-state) inspiral configuration. Shown are four different numerical resolutions, N1 (lowest) to N4 (highest), cf. Table II. Up to $t \sim 10\ M$, both mass and spin change by a few parts in 10^4, then they remain approximately constant (as indicated by the dashed horizontal lines) until shortly before merger. These steady-state values are used to define M and χ.

convergence of the different resolutions in the upper panel of Fig. 1. In the last $\sim 50\ M$ before merger, the mass increases slightly (seen as a vertical feature at the right edge of the plot), an effect we will discuss in more detail in the context of Fig. 5. The spin is likewise almost constant for $10 \lesssim t/M \lesssim 1000$, although some noise is visible for $t \lesssim 100\ M$.

We shall take the steady-state masses and spins evaluated at $t \sim 200\ M$ as the physical parameters of the binary being studied. Specifically, all dimensionful quantities will henceforth be expressed in terms of the mass scale M, which we define as the total mass *after* relaxation.

The relaxation of the black holes in the first $\sim 10\ M$ of the evolution is also accompanied by the emission of a pulse of unphysical junk radiation. This pulse passes through the computational domain, and leaves through the outer boundary after one light-crossing time. The junk radiation contains short wavelength features, which are not resolved in the wave zone. It turns out that the *constraint damping parameters* γ_0 and γ_2 (see [71]) influence how the unresolved junk radiation interacts with the numerical grid. Large constraint damping parameters enhance the conversion of the outgoing junk radiation (at the truncation error level) into incoming modes. This incoming radiation then lingers for several light-crossing times within the computational domain, imprinting noise into the extracted gravitational radiation. For small constraint damping parameters, this conversion is greatly suppressed, and numerical noise due to junk radiation diminishes much more rapidly. The simulations presented here use $\gamma_0 = \gamma_2 \sim 0.002\,25/M$ in the wave zone; these values are smaller by a factor of 100 than those used in [9,60]. (Even smaller constraint damping parameters fail to suppress constraint violations. Note that constraint damping parameters are much larger, $\gamma_0 = \gamma_2 \sim 3.56/M$, in the vicinity of the black holes.) The waveforms presented here show consequently reduced contaminations in the early part of the evolution and will be discussed in Sec. VI, cf. Fig. 15.

C. Inspiral

During the inspiral, the mapping between the comoving and inertial frames is chosen in the same way as in Refs. [9,60] and is denoted by $\mathcal{M}_I$: $x'^i \to x^i$, where primed coordinates denote the comoving frame and unprimed coordinates denote the inertial frame. Explicitly, this map is

$$r = \left[a(t) + (1 - a(t))\frac{r'^2}{R_0'^2}\right]r', \tag{4}$$

$$\theta = \theta', \tag{5}$$

$$\phi = \phi' + b(t), \tag{6}$$

where (r, θ, ϕ) and (r', θ', ϕ') denote spherical polar coordinates relative to the center of mass of the system in inertial and comoving coordinates, respectively. We choose $R_0' = 467\ M$. The functions $a(t)$ and $b(t)$ are determined by a dynamical control system as described in Ref. [89]. This control system adjusts $a(t)$ and $b(t)$ so that the centers of the apparent horizons remain stationary in the comoving frame.

While each hole is roughly in equilibrium during inspiral, we choose the gauge source function H_a in the same way as in Refs. [9,60]: A new quantity $\tilde{H}_a$ is defined that has the following two properties: (1) $\tilde{H}_a$ transforms like a tensor, and (2) in inertial coordinates $\tilde{H}_a = H_a$. H_a is chosen so that the constraint Eq. (3) is satisfied initially, and $\tilde{H}_{a'}$ is kept constant in the comoving frame, i.e.,

$$\partial_{t'}\tilde{H}_{a'} = 0. \tag{7}$$

D. Plunge

We make two key modifications to our algorithm to allow evolution through merger. The first is a change in gauge conditions, as in Ref. [60]. The second is a change in coordinate mappings that allows the excision boundaries to more closely track the horizons. We describe both of these changes here.

Following Ref. [60], at some time $t = t_g$ (where g stands for "gauge") we promote the gauge source function H_a to an independent dynamical field that satisfies

$$\nabla^c\nabla_c H_a = Q_a(x, t, \psi_{ab}) + \xi_2 t^b \partial_b H_a. \tag{8}$$

Here $\nabla^c\nabla_c$ is the curved space *scalar* wave operator (i.e. each component of H_a is evolved as a scalar), ψ_{ab} is the spacetime metric, and t^a is the timelike unit normal to the hypersurface. The driving functions Q_a are

$$Q_t = f(x, t)\xi_1 \frac{1 - N}{N^\eta}, \tag{9}$$

$$Q_i = g(x, t)\xi_3 \frac{\beta_i}{N^2}, \tag{10}$$

where N and β^i are the lapse function and the shift vector, η, ξ_1, ξ_2, and ξ_3 are constants, and $f(x, t)$ and $g(x, t)$ are prescribed functions of the spacetime coordinates. Equation (8) is evolved in first-order form, as described in Ref. [60]. Equation (8) requires values of H_a and its time derivative as initial data; these are chosen so that H_a and $\partial_t H_a$ are continuous at $t = t_g$.

This gauge is identical to the one used in Ref. [60], except that the parameters and functions that go into Eq. (8) are chosen slightly differently: We set $\eta = 4$, $\xi_1 = 0.1$, $\xi_2 = 6.5$, $\xi_3 = 0.01$, and

$$f(x, t) = (2 - e^{-(t-t_g)/\sigma_1})(1 - e^{-(t-t_g)^2/\sigma_2^2})e^{-r'^2/\sigma_3^2}, \tag{11}$$

$$g(x, t) = (1 - e^{-(t-t_g)/\sigma_4})(1 - e^{-(t-t_g)^2/\sigma_5^2})(t - t_g)e^{-r'^2/\sigma_3^2}, \tag{12}$$

where r' is the coordinate radius in comoving coordinates, and the constants are $\sigma_1 \sim 62\ M$, $\sigma_2 \sim 44.5\ M$, $\sigma_3 \sim 35\ M$, $\sigma_4 \sim 4.5\ M$, and $\sigma_5 \sim 3\ M$. The function $g(x, t)$ in Q_i, which drives the shift towards zero near the black holes, has a factor $(t - t_g)$ that is absent in Ref. [60]. Prescribing $g(x, t)$ in this way drives the shift towards zero more strongly at late times, which for this case is more effective in preventing gauge singularities from developing.

The second change we make at $t = t_g$ is to control the shape of each excision boundary so that it matches the shape of the corresponding apparent horizon. In the comoving frame, where the excision boundaries are spherical by construction, this means adjusting the coordinate mapping between the two frames such that the apparent horizons are also spherical. Without this "shape control," the horizons become sufficiently distorted with respect to the excision boundaries that the excision boundaries fail to remain outflow surfaces and our excision algorithm fails. For the nonspinning black hole binary in Ref. [60], shape control was not necessary before merger. To control the shape of black hole 1, we define the map $\mathcal{M}_{\rm AH1}$: $x'^i \rightarrow \tilde{x}^i$,

$$\tilde{\theta} = \theta', \tag{13}$$

$$\tilde{\phi} = \phi', \tag{14}$$

$$\tilde{r} \equiv r' - q_1(r') \sum_{\ell=0}^{\ell_{\max}} \sum_{m=-\ell}^{\ell} \lambda^1_{\ell m}(t) Y_{\ell m}(\theta', \phi'), \tag{15}$$

where

$$q_1(r') = e^{-(r' - r'_0(t))^3/\sigma_q^3}, \tag{16}$$

and (r', θ', ϕ') are spherical polar coordinates centered at the (fixed) comoving-coordinate location of black hole 1. The function $q_1(r')$ limits the action of the map to the vicinity of hole 1. The constant σ_q is chosen to be $\sim 4.5\ M$, and $r'_0(t) = r'_0 + \nu_1(t - t_g)^{2.1}$ is a function of time that approximately follows the radius of the black hole, with constants $r'_0 \sim 1.2\ M$ and $\nu_1 \sim 0.000\,46\ M$. Similarly, we define the map $\mathcal{M}_{\rm AH2}$ for black hole 2. Then the full map $\mathcal{M}_m$: $x'^i \rightarrow x^i$ from the comoving coordinates x'^i to the inertial coordinates x^i is given by

$$\mathcal{M}_m := \mathcal{M}_{\rm I} \circ \mathcal{M}_{\rm AH2} \circ \mathcal{M}_{\rm AH1}. \tag{17}$$

The functions $\lambda^1_{\ell m}(t)$ and $\lambda^2_{\ell m}(t)$ are determined by dynamical control systems as described in Refs. [60,89], so that the apparent horizons are driven to spheres (up to spherical harmonic component $l = l_{\max}$) in comoving coordinates. Note that $\mathcal{M}_{\rm AH1}$: $x'^i \rightarrow \tilde{x}^i$ is essentially the same map that we use to control the shape of the merged horizon

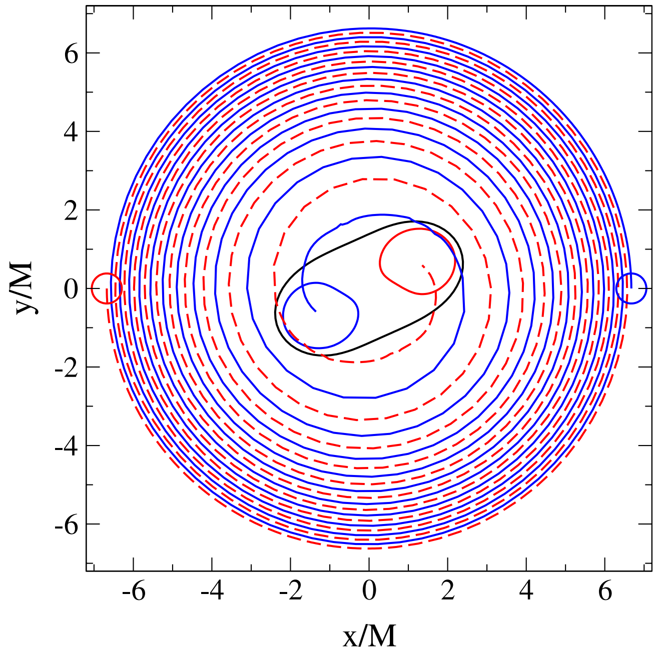

FIG. 2 (color online). Coordinate trajectories of the centers of the apparent horizons represented by the blue and red curves, up until the formation of a common horizon. The closed curves show the coordinate shapes of the corresponding apparent horizons.

during ringdown, and the control system for that map (and for the map $\mathcal{M}_{\rm AH2}$) is the same as the one described in Ref. [60] for controlling the shape of the merged horizon.

In addition to the modifications to the gauge conditions and coordinate map described above, the numerical resolution is also increased slightly around the two black holes during this more dynamical phase, and the evolution is continued until time t_m, shortly after the formation of a common horizon. The coordinate trajectories of the apparent horizon centers are shown in Fig. 2 up until t_m, at which point the binary has gone through 10.6 orbits.

E. Ringdown

Our methods for continuing the evolution once a common horizon has formed are the same as in Ref. [60]. After a common apparent horizon is found, all variables are interpolated onto a new computational domain that has only a single excised region. Then, a new comoving coordinate system (and a corresponding mapping to inertial coordinates) is chosen so that the new excision boundary tracks the shape of the apparent horizon in the inertial frame, and also ensures that the outer boundary behaves smoothly in time. The gauge conditions are modified as well: the shift vector is no longer driven to zero, so that the solution can relax to a time-independent state. This is done by allowing the gauge function $g(x, t)$ that appears in Eq. (10) to gradually approach zero; the gauge source function H_a still obeys Eqs. (8)–(10) as during the plunge.

Specifically, we change the functions $f(x, t)$ and $g(x, t)$ from Eqs. (11) and (12) to

$$f(x, t) = (2 - e^{-(t-t_g)/\sigma_1}) \times (1 - e^{-(t-t_g)^2/\sigma_2^2})e^{-r''^2/\sigma_3^2}, \tag{18}$$

$$g(x, t) = (1 - e^{-(t-t_g)/\sigma_4}) \times (1 - e^{-(t-t_g)^2/\sigma_5^2})(t - t_g) \times e^{-r''^2/\sigma_3^2} \times e^{-(t-t_m)/\sigma_6^2}, \tag{19}$$

where r'' is the coordinate radius in the new comoving coordinates, $\sigma_6 \sim 3.1\ M$, and t_m (here m stands for "merger") is the time we transition to the new domain decomposition.

IV. PROPERTIES OF THE NUMERICAL SOLUTIONS

A. Constraints

We do not explicitly enforce either the Einstein constraints or the secondary constraints that arise from writing the system in first-order form. Therefore, examining how well these constraints are satisfied provides a useful consistency check. Figure 3 shows the constraint violations for the evolutions at different resolutions. The top panel shows the L^2 norm of all the constraint fields of our first-order generalized harmonic system, normalized by the L^2 norm of the spatial gradients of the dynamical fields [see Eq. (71) of Ref. [71]]. The bottom panel shows the same quantity, but without the normalization factor [i.e., just the numerator of Eq. (71) of Ref. [71]]. The L^2 norms are taken over the portion of the computational volume that lies outside the apparent horizons.

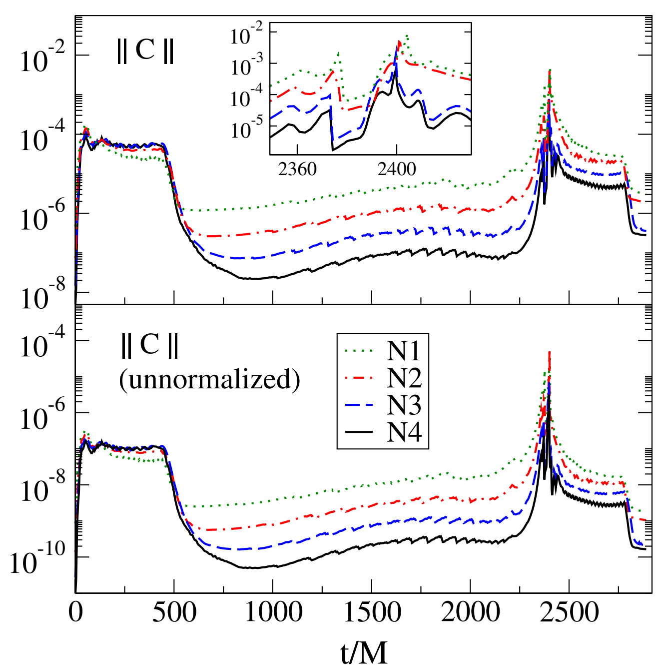

FIG. 3 (color online). Constraint violations of runs on different resolutions. The top panel shows the L^2 norm of all constraints, normalized by the L^2 norm of the spatial gradients of all dynamical fields. The bottom panel shows the same data, but without the normalization factor. The L^2 norms are taken over the portion of the computational volume that lies outside apparent horizons. Note that the time when we change the gauge before merger, $t_g \sim 2370\ M$, and the time when we regrid onto a new single-hole domain after merger, $t_m \sim 2400\ M$, are slightly different for different resolutions.

The constraints increase as the black holes approach each other and become increasingly distorted. At $t_g = 2372.05\ M$ for N4 ($t_g = 2372.05\ M$ for N3, $t_g = 2376.5\ M$ for N2, $t_g = 2376.5\ M$), the gauge conditions are changed (cf. Sec. III D) and the resolution around the holes is increased slightly. Because of the change in resolution, the constraints drop by more than an order of magnitude. Close to merger, the constraints grow larger again. The transition to a single-hole evolution (cf. Sec. III E) occurs at $t_m = 2399.64\ M$ for N4 ($t_m = 2399.66\ M$ for N3, $t_m = 2401.27\ M$ for N2, and $t_m = 2404.23\ M$ for N1). Shortly after this time, the constraints drop by about 2 orders of magnitude. This is because the largest constraint violations occur near and between the individual apparent horizons, and this region is newly excised from the computational domain at $t = t_m$.

B. Black hole spins and masses

There are different ways to compute the spin $\chi(t)$ of a black hole. The approach we prefer computes the spin from an angular momentum surface integral [66,67] using approximate Killing vectors of the apparent horizons, as described in [57,68] (see also [69,70]). We shall denote the resulting spin by $\chi_{\mathrm{AKV}}(t)$. Another less sophisticated method simply uses coordinate rotation vectors, and we denote the resulting spin by $\chi_{\mathrm{Coord}}(t)$. We also use two more spin diagnostics that are based on the minimum and maximum of the instrinsic scalar curvature of the apparent horizon for a Kerr black hole [57]; we call these $\chi_{\mathrm{SC}}^{\min}(t)$ and $\chi_{\mathrm{SC}}^{\max}(t)$. These last two measures of spin are expected to give reasonable results when the black holes are sufficiently far apart and close to equilibrium, and after the final black hole has settled down to a time-independent state. However, they are expected to be less accurate near merger and at the start of the evolution.

Figure 4 shows these four spin measures for black hole 1 in the N4 evolution during inspiral and plunge. From the lower left panel we see that $\chi_{\mathrm{SC}}^{\min}(t)$ and $\chi_{\mathrm{SC}}^{\max}(t)$ differ from $\chi_{\mathrm{Coord}}(t)$ and $\chi_{\mathrm{AKV}}(t)$ by more than a factor of 2 at $t = 0$. This indicates that the initial black holes do not have the appropriate shape for the Kerr solution; i.e. they are distorted because of the way the initial data is constructed. As the black holes relax, $\chi_{\mathrm{SC}}^{\min}(t)$ and $\chi_{\mathrm{SC}}^{\max}(t)$ approach the other two spin measures. The relaxed spin at $t \sim 200\ M$ is $\chi = 0.437\,57 \pm 0.000\,01$, where the uncertainty is

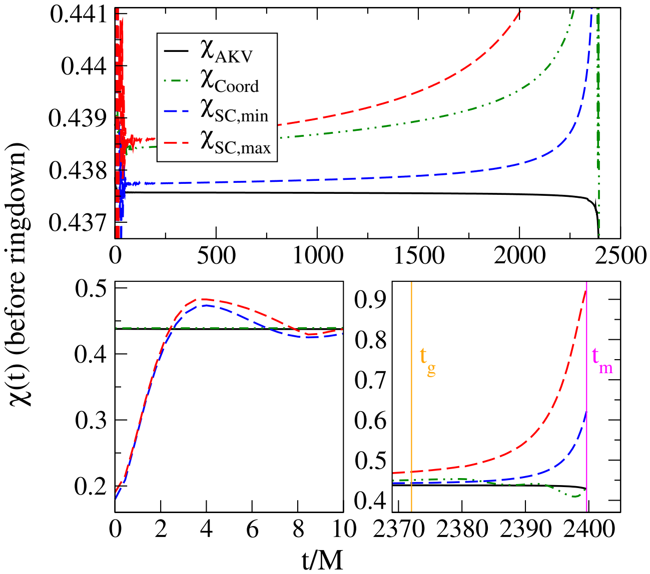

FIG. 4 (color online). Dimensionless spins χ of one black hole in the N4 evolution, evaluated using an approximate Killing vector, a coordinate rotation vector $-\partial_\phi$, or the extrema of the instrinsic scalar curvature on the apparent horizon. Bottom panels show detail at early and late times. Also shown are the time of gauge change t_g before merger, and the time t_m that we transition to a single-hole evolution just after merger.

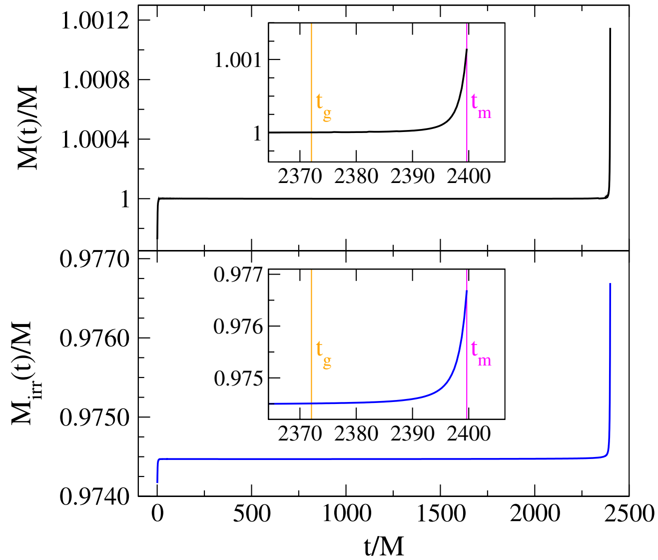

FIG. 5 (color online). Sum of Christodoulou masses $M(t)$ and sum of irreducible masses $M_{\rm irr}(t)$ of the two black holes during inspiral. The data is from the N4 evolution, and uses $\chi_{\rm AKV}$ when computing $M(t)$. Insets show detail at late times, and indicate the transition times t_g and t_m.

based on the variation in $\chi_{\rm AKV}$ between $t = 100\ M$ and $t = 1000\ M$. During the inspiral, $\chi_{\rm AKV}(t)$ decreases slowly and monotonically, dropping by 10^{-4} at 90 M before merger, and dropping by 0.01 at the time of merger. Tidal dissipation should *slow down* the black holes, so this decrease is physically sensible. In contrast, the other three spin diagnostics show a mild *increase* in spin, suggesting that they are less reliable. Close to merger, $\chi_{\rm SC}^{\rm min}(t)$ and $\chi_{\rm SC}^{\rm max}(t)$ increase dramatically, with $\chi_{\rm SC}^{\rm max}(t)$ growing as large as 0.92. In this regime, the shapes of the individual black holes are dominated by tidal distortion, and are therefore useless for measuring the spin.

The Christodoulou mass m of one black hole, as defined in Eq. (1), depends on the spin. We take $\chi_{\rm AKV}(t)$ as the preferred spin measure, and use it to compute the total Christodoulou mass $M(t)$ during the inspiral and plunge. This is shown in the top panel of Fig. 5. The Christodoulou mass settles down to $M(t)/M = 1.000\,000$ after $t = 150\ M$ (this defines M), and increases to $M(t)/M = 1.001\,14$ at the time of merger. Most of the increase in mass occurs very close to merger, as can be seen from the inset of Fig. 5. Until about 30 M before merger (i.e. $t = 2370\ M$), the mass is constant to a few parts in 10^6. For comparison, in the bottom panel we also display $M_{\rm irr}(t)$, the sum of the irreducible masses, which does not depend on the spin. This quantity settles down to $M_{\rm irr}(t)/M = 0.974\,508$ at $t = 200\ M$, and increases to $M_{\rm irr}(t)/M = 0.976\,68$ at $t = 2400\ M$. Again, almost all of this increase happens shortly before merger. During the inspiral up to 30 M before merger, $M_{\rm irr}(t)/M$ increases by only 6×10^{-5}, but in the last 30 M the increase is $\sim$0.002.

The merger results in one highly distorted black hole, which subsequently rings down into a stationary Kerr black hole. Figure 6 shows our four spin diagnostics during the

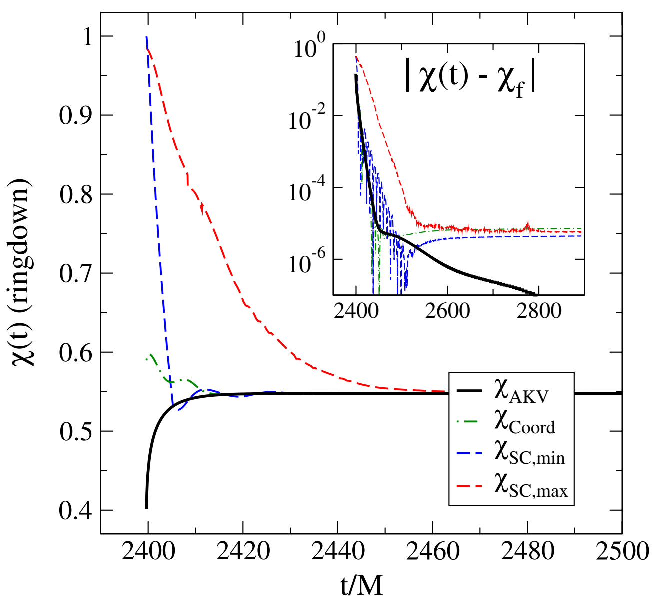

FIG. 6 (color online). Dimensionless spins $\chi(t)$ of the final black hole in the N4 evolution. The (most reliable) spin diagnostic $\chi_{\rm AKV}$ starts at $\sim$0.4 and increases to its final value $\chi_f = 0.547\,81 \pm 0.000\,01$. The other spin diagnostics are unreliable for the highly distorted black hole shortly after merger, but subsequently approach $\chi_{\rm AKV}$.

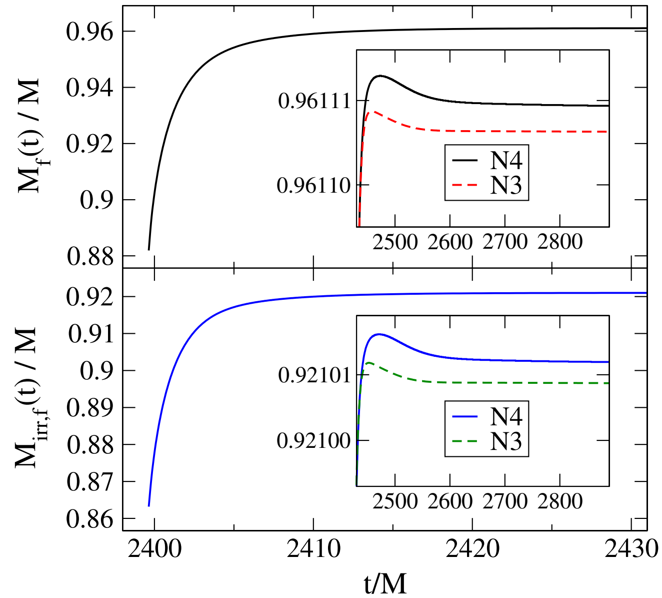

FIG. 7 (color online). The top panel shows the Christodoulou mass $M_f(t)$ of the final black hole in the N4 and N3 runs, computed using $\chi_{\mathrm{AKV}}(t)$. The bottom panel shows the irreducible mass $M_{\mathrm{irr,f}}(t)$.

ringdown. The spin measures $\chi_{\mathrm{SC}}^{\min}(t)$ and $\chi_{\mathrm{SC}}^{\max}(t)$ assume a Kerr black hole. Just after merger, the horizon is highly distorted, so these two spin diagnostics are not valid there. However, as the remnant black hole rings down to Kerr, $\chi_{\mathrm{SC}}^{\max}(t)$ and $\chi_{\mathrm{SC}}^{\min}(t)$ approach the quasilocal AKV spin to better than 1 part in 10^5 (see the inset of Fig. 6). The quasilocal spin based on coordinate rotation vectors, $\chi_{\mathrm{Coord}}(t)$, also agrees with the other spin measures to a similar level at late times. The spin of the final black hole points in the direction of the initial orbital angular momentum.

The Christodoulou mass $M_f(t)$ of the final black hole in the N4 evolution, again evaluated using $\chi_{\mathrm{AKV}}(t)$, is shown in the top panel of Fig. 7. The mass settles down to a final value of $M_f/M = 0.961\,109 \pm 0.000\,003$. The bottom panel shows the irreducible mass $M_{\mathrm{irr,f}}(t)$ of the final black hole, which settles down to a final value of $M_{\mathrm{irr,f}} = 0.921\,012 \pm 0.000\,003$. The uncertainties are determined from the difference between runs N4 and N3, so they include only numerical truncation error and not any systematic effects. The uncertainty in the mass is visible in the insets of Fig. 7.

V. COMPUTATION OF THE WAVEFORM

A. Waveform extraction

Gravitational waves are extracted from the simulation on spheres of different values of the coordinate radius r, following the same procedure as in Refs. [60,65,90]. The Newman-Penrose scalar Ψ_4 in terms of spin-weighted spherical harmonics of weight 2

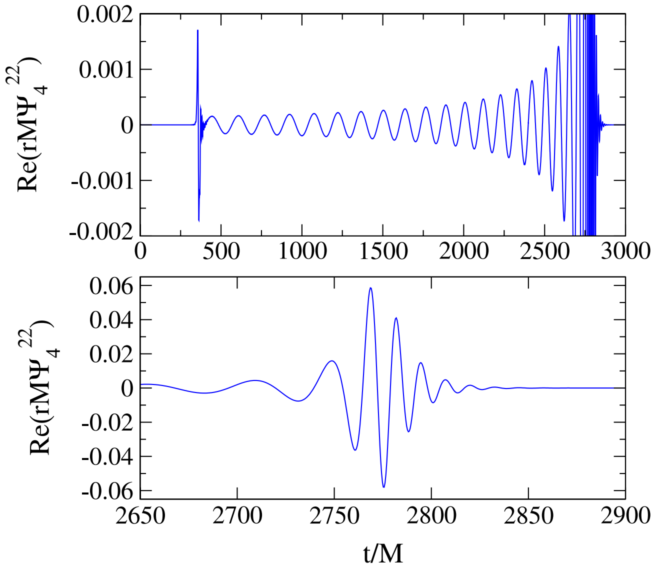

FIG. 8 (color online). Gravitational waveform extracted at finite radius $r = 350\ M$ for the N4 evolution. The top panel zooms in on the inspiral waveform, and the bottom panel zooms in on the merger and ringdown.

$$\Psi_4(t, r, \theta, \phi) = \sum_{lm} \Psi_4^{lm}(t, r)\,{}_{-2}Y_{lm}(\theta, \phi), \tag{20}$$

where the Ψ_4^{lm} are expansion coefficients defined by this equation. Here we also focus on the dominant $(l, m) = (2, 2)$ mode, and split the extracted waveform into real phase ϕ and real amplitude A, defined by (see e.g. [3,91])

$$\Psi_4^{22}(r, t) = A(r, t)e^{-i\phi(r,t)}. \tag{21}$$

The gravitational wave frequency is given by

$$\omega = \frac{d\phi}{dt}. \tag{22}$$

The minus sign in Eq. (21) is chosen so that the phase increases in time and ω is positive.

The coordinate radius of our outer boundary is located at $R_{\max} = 427\ M$ at $t = 0$ and $R_{\max} = 365\ M$ at $t > 2500\ M$; it shrinks slightly during the evolution because of the mappings [cf. Equation (4)] used in our dual frame approach. The $(l, m) = (2, 2)$ waveform, extracted at a single coordinate radius $r = 350\ M$ for the N4 evolution, is shown in Fig. 8. The short pulse at $t \sim 360\ M$ is due to junk radiation. The magnitude of this pulse is about twice as large as for nonspinning black holes, cf. Ref. [9,60].

B. Convergence of extracted waveforms

In this section we examine the convergence of the gravitational waveforms extracted at fixed radius, without extrapolation to infinity. This allows us to study the behavior of our code without the complications of extrapolation. The extrapolation process and the resulting extrapolated waveforms are discussed in Sec. V C.

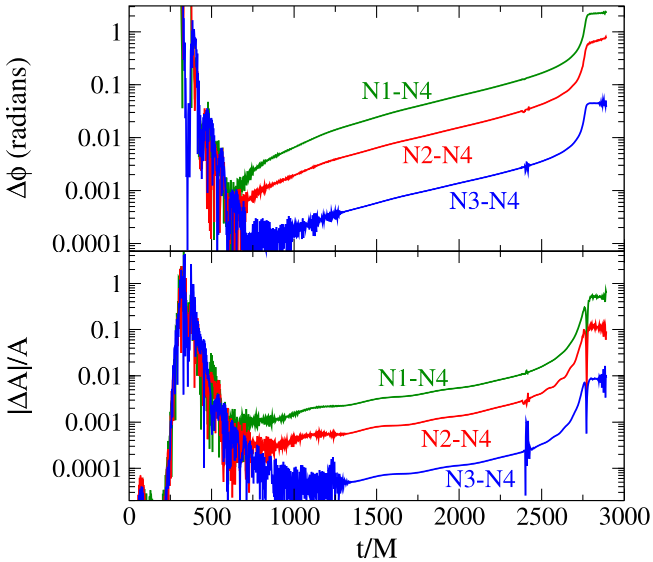

FIG. 9 (color online). Convergence of gravitational waveforms with numerical resolution. Shown are phase and amplitude differences between numerical waveforms Ψ_4^{22} computed using different numerical resolutions. All waveforms are extracted at $r = 350\ M$, and no time shifting or phase shifting is done to align waveforms.

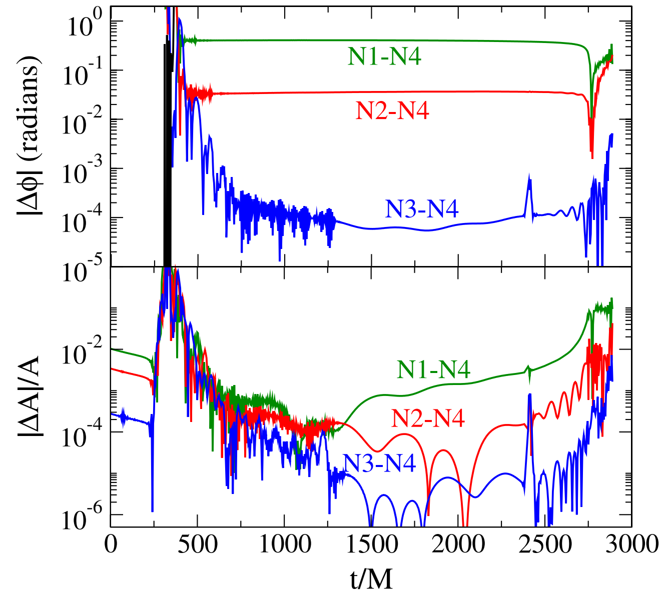

FIG. 10 (color online). Convergence of gravitational waveforms with numerical resolution. The same as Fig. 9 except all other waveforms are time- shifted and phase shifted to best match the waveform of the N4 run.

Figure 9 shows the convergence of the gravitational wave phase ϕ and amplitude A with numerical resolution. For this plot, the waveform was extracted at a fixed inertial-coordinate radius of $r = 350\ M$. Each line in the top panel shows the absolute difference between ϕ computed at some particular resolution and ϕ computed from our highest resolution N4 run. The curves in the bottom panel similarly show the *relative* amplitude differences. When subtracting results at different resolutions, no time or phase adjustment has been performed. The noise at early times is due to junk radiation generated near $t = 0$. Most of this junk radiation leaves through the outer boundary after one crossing time. The plots show that the phase difference accumulated over 10.6 orbits plus merger and ringdown—in total 31 gravitational wave cycles—is less than 0.1 radians, and the relative amplitude differences are less than 0.017. These numbers can be taken as an estimate of the numerical truncation error of our N3 run. Because of the rapid convergence of the code, we expect that the errors of the N4 run are significantly smaller.

Figure 10 is the same as Fig. 9 after the N1, N2, N3 waveforms have been time shifted and phase shifted to best match the waveform of the N4 evolution. This best match is determined by a simple least-squares procedure: we minimize the function

$$\sum_i (A_1(t_i)e^{i\phi_1(t_i)} - A_2(t_i + t_0)e^{i(\phi_2(t_i+t_0)+\phi_0)})^2, \qquad (23)$$

by varying t_0 and ϕ_0. Here A_1, ϕ_1, A_2, and ϕ_2 are the amplitudes and phases of the two waveforms being matched, and the sum goes over all times t_i at which waveform 1 is sampled. This type of comparison is relevant for analysis of data from gravitational wave detectors: when comparing experimental data with numerical detection templates, the template will be shifted in both time and phase to best match the data. For this type of comparison, Fig. 10 shows that the numerical truncation error of our N3 run is less than 0.01 radians in phase and 0.1% in amplitude for $t > 550\ M$. At earlier times, the errors are somewhat larger and are dominated by residual junk radiation.

C. Extrapolation of waveforms to infinity

Gravitational wave detectors measure waveforms as seen by an observer effectively infinitely far from the source. Since our numerical simulations cover only a finite spacetime volume, after extracting waveforms at multiple finite radii, we extrapolate these waveforms to infinite radius using the procedure described in [60] (see also [90] for more details). This is intended to reduce near-field effects as well as gauge effects that can be caused by the time dependence of the lapse function or the nonoptimal choice of tetrad for computing Ψ_4.

The extrapolation of the extracted waveforms involves first computing each extracted waveform as a function of retarded time $u = t_s - r^*$ and extraction radius $r_{\rm areal}$ (see [60] for precise definitions). Then at each value of u, the phase and amplitude are fitted to polynomials in $1/r_{\rm areal}$:

$$\phi(u, r_{\rm areal}) = \phi_{(0)}(u) + \sum_{k=1}^{n} \frac{\phi_{(k)}(u)}{r_{\rm areal}^k}, \qquad (24)$$

$$r_{\text{areal}} A(u, r_{\text{areal}}) = A_{(0)}(u) + \sum_{k=1}^{n} \frac{A_{(k)}(u)}{r_{\text{areal}}^k}. \tag{25}$$

The phase and amplitude of the desired asymptotic waveform are thus given by the leading-order term of the corresponding polynomial, as a function of retarded time:

$$\phi(u) = \phi_{(0)}(u), \tag{26}$$

$$r_{\text{areal}} A(u) = A_{(0)}(u). \tag{27}$$

Figure 11 shows phase and amplitude differences between extrapolated waveforms that are computed using different values of polynomial order n in Eqs. (24) and (25). The extrapolation is based on waveforms extracted at 20 different radii between 75 M and 350 M. As in [60], our preferred extrapolation order is $n = 3$, which gives a phase error of less than 0.004 radians and a relative amplitude error of less than 0.006 during most of the inspiral, and a phase error of less than 0.01 radians and a relative amplitude error of 0.006 in the ringdown.

Figure 12 is the same as the top panel of Fig. 11, except zoomed to late times. During merger and ringdown, the extrapolation procedure does not converge with increasing extrapolation order n: the phase differences are slightly larger for larger n. This was also seen for the extrapolated waveforms of our equal-mass nonspinning black hole binary [60], and is possibly due to gauge effects that do not obey the fitting formulas, Eqs. (24) and (25).

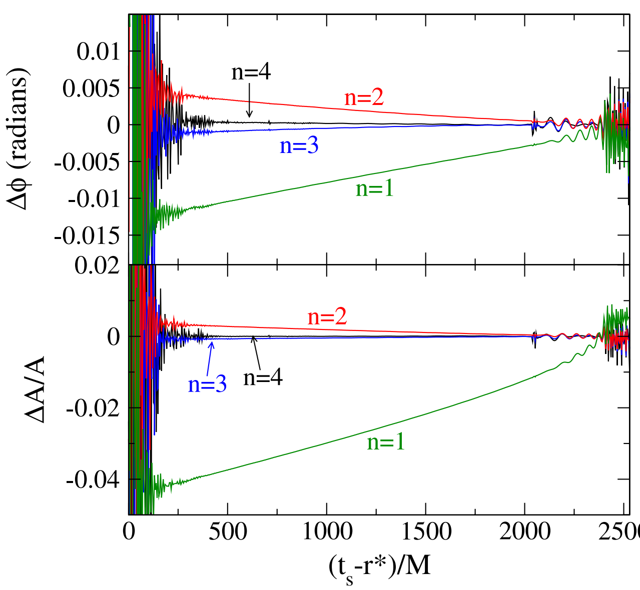

FIG. 11 (color online). Convergence of extrapolation to infinity for extrapolation of order n. For each n, plotted is the extrapolated waveform from N4 using order $n + 1$ minus the extrapolated waveform using order n. The top panel shows phase differences, the bottom panel shows amplitude differences. No shifting in time or phase has been done for this comparison.

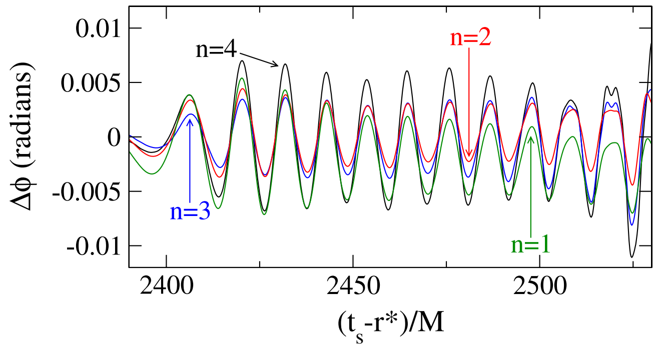

FIG. 12 (color online). Late-time phase convergence of extrapolation to infinity. The same as the top panel of Fig. 11, except zoomed to late times. The peak amplitude of the waveform occurs at $t_s - r^* = 2410.6\ M$.

Figure 13 shows the phase and amplitude differences between our preferred extrapolated waveform using $n = 3$ and the waveform extrapolated at coordinate radius $r = 350\ M$, both for the N4 run. The extrapolated waveform has been shifted in time and phase so as to best match the $n = 3$ extrapolated waveform, using the least-squares fit of Eq. (23). The phase difference between the extrapolated waveform and the waveform extracted at $r = 350\ M$ becomes as large as 0.13 radians, and the amplitude difference is on the order of 1%.

Figure 14 presents the final waveform after extrapolation to infinite radius. There are 22 gravitational wave cycles before the maximum of $|\Psi_4|$, and 9 gravitational wave

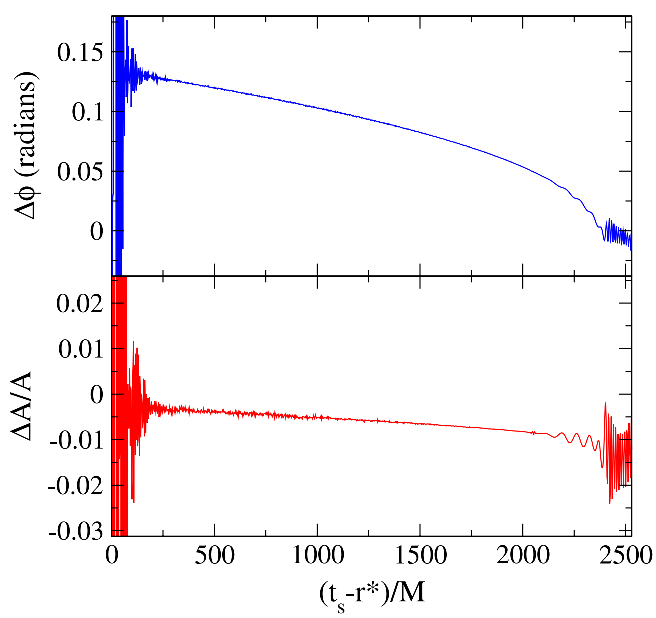

FIG. 13 (color online). Phase and relative amplitude differences between extrapolated and extracted waveforms for N4. The extracted waveform is extracted at coordinate radius $r = 350M$. The waveforms are time-shifted and phase-shifted to produce the best least-squares match.

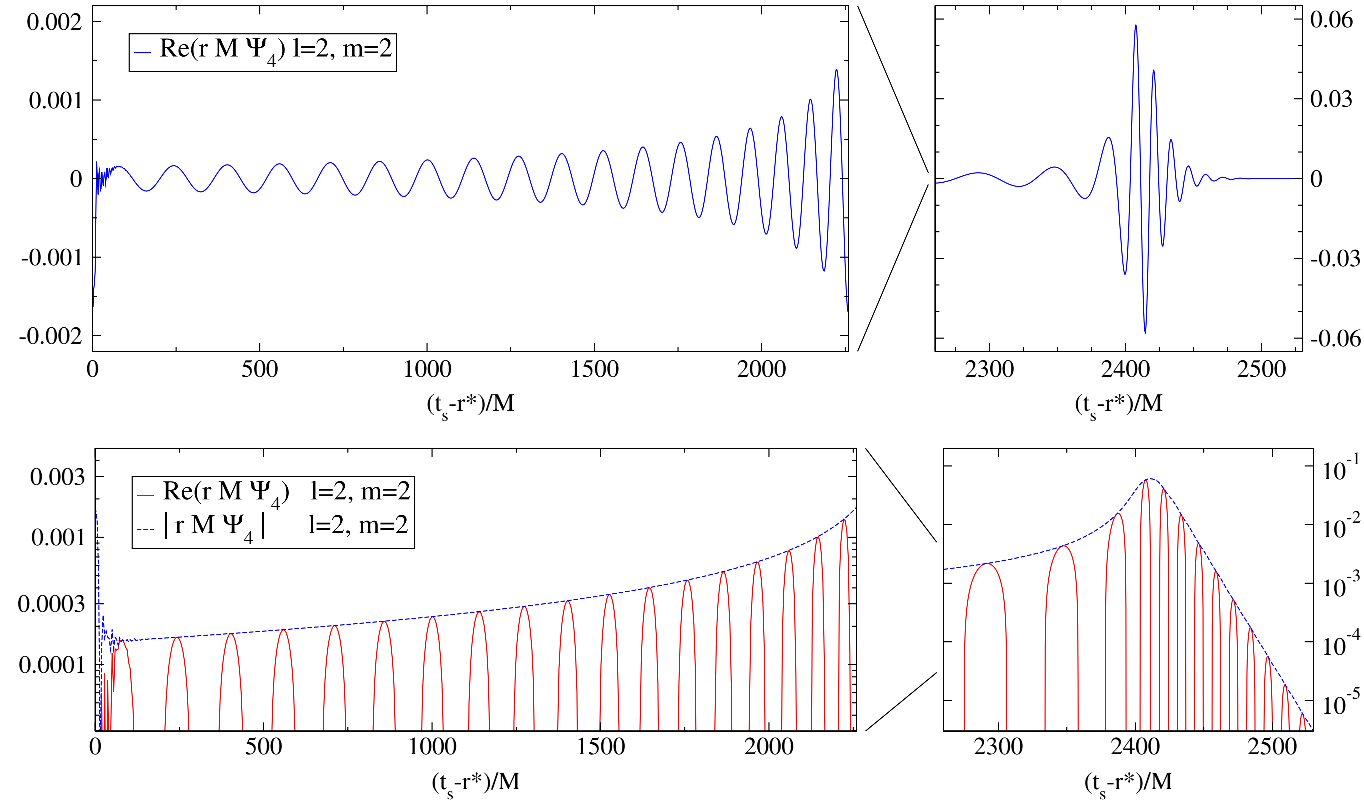

FIG. 14 (color online). Final waveform, extrapolated to infinity. The top panels show the real part of Ψ_4^{22} with a linear y-axis, the bottom panels with a logarithmic y-axis. The right panels show an enlargement of merger and ringdown.

cycles during ringdown, over which the amplitude of $|\Psi_4|$ drops by 4 orders of magnitude.

VI. DISCUSSION

We have presented the first spectral computation of a binary black hole inspiral, merger, and ringdown with spinning black holes, and find that we can achieve similar accuracy for the final mass, final spin, and gravitational waveforms as in the nonspinning case [60]. For initial spins of $\chi = 0.437\,57 \pm 0.000\,01$, the mass and spin of the final hole are $M_f/M = 0.961\,109 \pm 0.000\,003$ and $\chi_f = 0.547\,81 \pm 0.000\,01$. The uncertainties are based on comparing runs at our highest two resolutions, and do not take into account systematic errors (e.g. the presence of a finite outer boundary or gauge effects). Note that for the nonspinning case [60], we found that changing the outer boundary location produced a smaller effect on the final mass and spin than changing the resolution, and that the outer boundary for the evolutions presented here is more distant (at late times, when most of the radiation passes through the boundary) than it was in Ref. [60]. The uncertainties in the gravitational waveforms are $\lesssim 0.01$ radians in phase and $\lesssim 0.6$ percent in amplitude (when waveforms are time and phase shifted). These uncertainties are based on comparisons between our two highest resolution runs and comparisons between different methods of extrapolating waveforms to infinite extraction radius.

The methods used here to simulate plunge and ringdown are similar to those in Ref. [60]. The primary disadvantage of these methods is that they require fine tuning during the plunge (Sec. III D). For example, the function $g(x, t)$ defined in Eq. (12) must be chosen carefully or else the simulation fails shortly (a few M) before a common horizon forms. There are at least two reasons that fine tuning is currently necessary. First, the gauge conditions must be chosen so that no coordinate singularities occur before merger. Second, the excision boundaries do not coincide with the apparent horizons, but instead they lie somewhat inside the horizons. If the excision boundaries exactly followed the horizons, then the characteristic fields of the system would be guaranteed to be outflowing (into the holes) at the excision boundaries, so that no boundary condition is required there. But for excision boundaries inside the horizons, the outflow condition depends on the location of the excision boundary, its motion with respect to the horizon, and the gauge. Indeed, the most common mode of failure for improperly-tuned gauge parameters is that the outflow condition fails at some point on one of the excision boundaries. We have been working on improved gauge conditions [92] and on improved algorithms for allowing the excision boundary to more closely track the

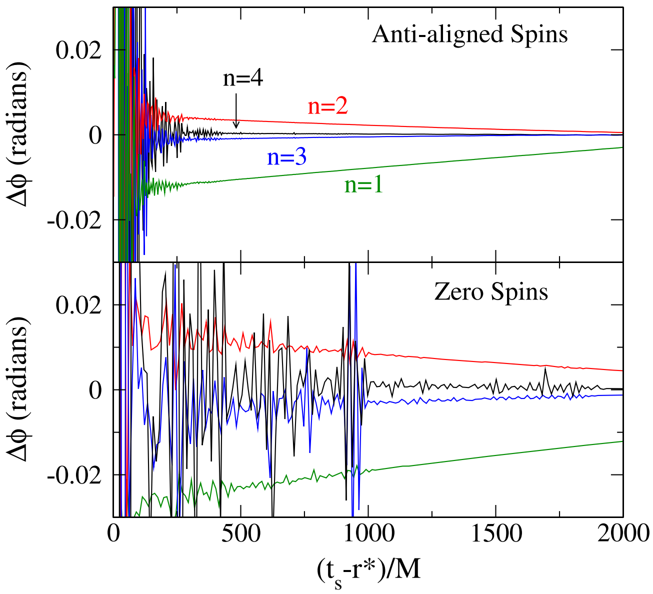

FIG. 15 (color online). Comparison of waveform extrapolation between the current simulation of counter-rotating black holes (top panel), and the earlier simulation of nonspinning black holes [9,60]. The noise is significantly reduced in the newer simulation, due to smaller constraint damping parameters in the wave zone.

apparent horizon. These and other improvements greatly reduce the amount of necessary fine tuning and allow mergers in generic configurations, and will be described in detail elsewhere [93].

Another quite important improvement lies in the choice of constraint damping parameters. To illustrate this effect, Fig. 15 compares the gravitational wave phase extrapolation for the simulation presented here with the similar plot for an earlier run [9] with different constraint damping parameters. As can be seen in Fig. 15, the improved constraint damping parameters result in significantly reduced noise. For the earlier simulation, the waveform was unusable for $t - r^* < 1000\ M$, and was still noticeably noisy at $1000\ M < t - r^* < 2000\ M$. For the new simulation, the smaller constraint damping parameters result in clean waveforms as early as $t - r^* \sim 250\ M$, despite the observation that the spinning black holes result in a pulse of junk radiation of about twice the amplitude of the earlier run. The new simulation also shows smaller extrapolation errors, presumably because the new simulation uses larger extraction radii (up to $r = 350\ M$, whereas Ref. [9] uses a largest extraction radius of $r = 240\ M$).

We employ four techniques to measure black hole spin: Two of these are based on the surface integral for quasilocal linear momentum, and utilize either simple coordinate rotation vectors $\chi_{\rm Coord}(t)$ or approximate Killing vectors, $\chi_{\rm AKV}(t)$; the other two are based on the shape of the apparent horizon, and infer the spin from the extrema of the scalar curvature [$\chi^{\rm min}_{\rm SC}(t)$, $\chi^{\rm max}_{\rm SC}(t)$]. The four spin measures agree to better than 1% during the inspiral. The AKV

TABLE III. Predictions of final black hole spin and mass from analytical formulas in the literature, applied to the simulation considered here. References [97,98] do not predict the final mass, but instead assume zero mass loss.

Prediction Formula	χ_f	M_f/M
Kesden [99]	0.521 153	0.970 39
Buonanno, Kidder, and Lehner [97]	0.505 148	1.0
Tichy and& Marronetti [100]	0.548 602	0.962 877
Boyle and Kesden [101]	0.547 562	0.964 034
Barausse and Rezzolla [98]	0.546 787	1.0
Numerical Result (This Paper)	0.547 81	0.961 109

spin $\chi_{\rm AKV}(t)$ shows the least variations during the simulation, and is the only spin diagnostic that results in a monotonically decreasing spin during the inspiral, as expected from the effects of tidal friction. These results may be compared with those that can be found from tidal multipole moments (e.g. [94–96]), which we defer to future work. The other three spin measures [$\chi_{\rm coord}(t)$, $\chi^{\rm max}_{\rm SC}(t)$, $\chi^{\rm min}_{\rm SC}(t)$] show various undesired and physically unreasonable behaviors: All three result in *increasing* spin during the inspiral, inconsistent with tidal friction (cf. Fig. 4). $\chi^{\rm min}_{\rm SC}(t)$ and $\chi^{\rm max}_{\rm SC}(t)$, furthermore show very strong variations during the initial transients, just before merger, and just after the common horizon forms. This is expected, as in those regions of the evolution, the black holes can not be approximated as isolated Kerr black holes. The behavior of $\chi^{\rm min}_{\rm SC}(t)$ and $\chi^{\rm max}_{\rm SC}(t)$ contain information about the deformation of the black holes. The final state of the simulation is expected to be a single, stationary Kerr black hole, for which $\chi^{\rm min}_{\rm SC}(t)$ and $\chi^{\rm max}_{\rm SC}(t)$ should result in the correct spin. Indeed, all four spin diagnostics agree at very late time to five significant digits (cf. Fig. 6). The accuracy of our simulation places new constraints on analytic formulas that predict the final black hole spin from the initial spins and masses of a black hole binary. Table III lists some of these predictions.

ACKNOWLEDGMENTS

We would like to thank Lee Lindblom, Béla Szilágyi, and Kip Thorne for helpful discussions and comments. We thank Mike Kesden for computing the final mass and spin predictions from the various analytical models. We are especially grateful to Fan Zhang for computing the extrapolation of the waveforms to infinite radius using methods and a variant of code developed by Mike Boyle and Abdul Mroue. We acknowledge the use of the Spectral Einstein Code (SpEC). This work was supported in part by the Sherman Fairchild Foundation, the Brinson Foundation, by NSF grants PHY-0601459, PHY-0652995, and DMS-0553302 and by NASA grant NNX09AF97G. H. P. acknowledges support from the Canadian Institute for Advanced Research. Some calculations were done on the Tungsten cluster at NCSA.

[1] F. Pretorius, Phys. Rev. Lett. **95**, 121101 (2005).
[2] M. Campanelli, C. O. Lousto, P. Marronetti, and Y. Zlochower, Phys. Rev. Lett. **96**, 111101 (2006).
[3] J. G. Baker, J. Centrella, D.-I. Choi, M. Koppitz, and J. van Meter, Phys. Rev. Lett. **96**, 111102 (2006).
[4] A. Buonanno, G. B. Cook, and F. Pretorius, Phys. Rev. D **75**, 124018 (2007).
[5] J. G. Baker, J. R. van Meter, S. T. McWilliams, J. Centrella, and B. J. Kelly, Phys. Rev. Lett. **99**, 181101 (2007).
[6] Y. Pan, A. Buonanno, J. G. Baker, J. Centrella, B. J. Kelly, S. T. McWilliams, F. Pretorius, and J. R. van Meter, Phys. Rev. D **77**, 024014 (2008).
[7] A. Buonanno, Y. Pan, J. G. Baker, J. Centrella, B. J. Kelly, S. T. McWilliams, and J. R. van Meter, Phys. Rev. D **76**, 104049 (2007).
[8] M. Hannam, S. Husa, J. A. González, U. Sperhake, and B. Brügmann, Phys. Rev. D **77**, 044020 (2008).
[9] M. Boyle, D. A. Brown, L. E. Kidder, A. H. Mroué, H. P. Pfeiffer, M. A. Scheel, G. B. Cook, and S. A. Teukolsky, Phys. Rev. D **76**, 124038 (2007).
[10] A. Gopakumar, M. Hannam, S. Husa, and B. Brügmann, Phys. Rev. D **78**, 064026 (2008).
[11] M. Hannam, S. Husa, B. Brügmann, and A. Gopakumar, Phys. Rev. D **78**, 104007 (2008).
[12] T. Damour, A. Nagar, E. N. Dorband, D. Pollney, and L. Rezzolla, Phys. Rev. D **77**, 084017 (2008).
[13] T. Damour and A. Nagar, Phys. Rev. D **77**, 024043 (2008).
[14] M. Boyle, A. Buonanno, L. E. Kidder, A. H. Mroué, Y. Pan, H. P. Pfeiffer, and M. A. Scheel, Phys. Rev. D **78**, 104020 (2008).
[15] A. H. Mroué, L. E. Kidder, and S. A. Teukolsky, Phys. Rev. D **78**, 044004 (2008).
[16] I. Hinder, F. Herrmann, P. Laguna, and D. Shoemaker, arXiv:0806.1037, http://www.arxiv.org/abs/0806.1037.
[17] T. Damour, A. Nagar, M. Hannam, S. Husa, and B. Brügmann, Phys. Rev. D **78**, 044039 (2008).
[18] T. Damour and A. Nagar, Phys. Rev. D **79**, 081503 (2009).
[19] A. Buonanno, Y. Pan, H. P. Pfeiffer, M. A. Scheel, L. T. Buchman, and L. E. Kidder, Phys. Rev. D **79**, 124028 (2009).
[20] M. Campanelli, Classical Quantum Gravity **22**, S387 (2005).
[21] F. Herrmann, I. Hinder, D. Shoemaker, and P. Laguna, Classical Quantum Gravity **24**, S33 (2007).
[22] J. G. Baker, J. Centrella, D.-I. Choi, M. Koppitz, J. R. van Meter, and M. C. Miller, Astrophys. J. **653**, L93 (2006).
[23] J. A. Gonzalez, U. Sperhake, B. Brügmann, M. Hannam, and S. Husa, Phys. Rev. Lett. **98**, 091101 (2007).
[24] M. Campanelli, C. O. Lousto, Y. Zlochower, and D. Merritt, Phys. Rev. Lett. **98**, 231102 (2007).
[25] J. A. Gonzalez, M. D. Hannam, U. Sperhake, B. Brügmann, and S. Husa, Phys. Rev. Lett. **98**, 231101 (2007).
[26] B. Brügmann, J. A. González, M. Hannam, S. Husa, and U. Sperhake, Phys. Rev. D **77**, 124047 (2008).
[27] F. Herrmann, I. Hinder, D. Shoemaker, P. Laguna, and R. A. Matzner, Astrophys. J. **661**, 430 (2007).
[28] F. Herrmann, I. Hinder, D. M. Shoemaker, P. Laguna, and R. A. Matzner, Phys. Rev. D **76**, 084032 (2007).
[29] D.-I. Choi, B. J. Kelly, W. D. Boggs, J. G. Baker, J. Centrella, and J. van Meter, Phys. Rev. D **76**, 104026 (2007).
[30] J. G. Baker, W. D. Boggs, J. Centrella, B. J. Kelly, S. T. McWilliams, M. C. Miller, and J. R. van Meter, Astrophys. J. **668**, 1140 (2007).
[31] W. Tichy and P. Marronetti, Phys. Rev. D **76**, 061502(R) (2007).
[32] J. D. Schnittman, A. Buonanno, J. R. van Meter, J. G. Baker, W. D. Boggs, J. Centrella, B. J. Kelly, and S. T. McWilliams, Phys. Rev. D **77**, 044031 (2008).
[33] M. Campanelli, C. O. Lousto, Y. Zlochower, and D. Merritt, Astrophys. J. Lett. **659**, L5 (2007).
[34] M. Koppitz, D. Pollney, C. Reisswig, L. Rezzolla, J. Thornburg, P. Diener, and E. Schnetter, Phys. Rev. Lett. **99**, 041102 (2007).
[35] S. H. Miller and R. Matzner, Gen. Relativ. Gravit. **41**, 525 (2009).
[36] J. G. Baker, W. D. Boggs, J. Centrella, B. J. Kelly, S. T. McWilliams, M. C. Miller, and J. R. van Meter, Astrophys. J. **682**, L29 (2008).
[37] J. Healy, F. Herrmann, I. Hinder, D. M. Schoemaker, P. Laguna, and R. A. Matzner, Phys. Rev. Lett. **102**, 041101 (2009).
[38] L. Rezzolla *et al.*, Astrophys. J. **679**, 1422 (2008).
[39] M. Campanelli, C. O. Lousto, and Y. Zlochower, Phys. Rev. D **74**, 041501 (2006).
[40] M. Campanelli, C. O. Lousto, and Y. Zlochower, Phys. Rev. D **74**, 084023 (2006).
[41] M. Campanelli, C. O. Lousto, Y. Zlochower, B. Krishnan, and D. Merritt, Phys. Rev. D **75**, 064030 (2007).
[42] P. Marronetti, W. Tichy, B. Brügmann, J. González, and U. Sperhake, Phys. Rev. D **77**, 064010 (2008).
[43] E. Berti, V. Cardoso, J. A. Gonzalez, U. Sperhake, and B. Brügmann, Classical Quantum Gravity **25**, 114035 (2008).
[44] L. S. Finn, Phys. Rev. D **46**, 5236 (1992).
[45] S. Bonazzola, J. Frieben, E. Gourgoulhon, and J.-A. Marck, in *ICOSAHOM'95, Proceedings of the Third International Conference on Spectral and High Order Methods*, edited by A. V. Ilin and L. R. Scott (Houston Journal of Mathematics, Houston, 1996), p. 3–19.
[46] S. Bonazzola, E. Gourgoulhon, and J.-A. Marck, Phys. Rev. Lett. **82**, 892 (1999).
[47] P. Grandclément, S. Bonazzola, E. Gourgoulhon, and J.-A. Marck, J. Comput. Phys. **170**, 231 (2001).
[48] E. Gourgoulhon, P. Grandclément, and S. Bonazzola, Phys. Rev. D **65**, 044020 (2002).
[49] P. Grandclément, E. Gourgoulhon, and S. Bonazzola, Phys. Rev. D **65**, 044021 (2002).
[50] H. P. Pfeiffer, G. B. Cook, and S. A. Teukolsky, Phys. Rev. D **66**, 024047 (2002).
[51] H. P. Pfeiffer, L. E. Kidder, M. A. Scheel, and S. A. Teukolsky, Comput. Phys. Commun. **152**, 253 (2003).
[52] G. B. Cook and H. P. Pfeiffer, Phys. Rev. D **70**, 104016 (2004).
[53] M. Ansorg, B. Brügmann, and W. Tichy, Phys. Rev. D **70**, 064011 (2004).
[54] M. Ansorg, Phys. Rev. D **72**, 024018 (2005).
[55] M. Caudill, G. B. Cook, J. D. Grigsby, and H. P. Pfeiffer, Phys. Rev. D **74**, 064011 (2006).
[56] P. Grandclément, Phys. Rev. D **74**, 124002 (2006).

[57] G. Lovelace, R. Owen, H. P. Pfeiffer, and T. Chu, Phys. Rev. D **78**, 084017 (2008).
[58] F. Foucart, L. E. Kidder, H. P. Pfeiffer, and S. A. Teukolsky, Phys. Rev. D **77**, 124051 (2008).
[59] L. T. Buchman, H. P. Pfeiffer, and J. M. Bardeen, Phys. Rev. D **80**, 084024 (2009).
[60] M. A. Scheel, M. Boyle, T. Chu, L. E. Kidder, K. D. Matthews, and H. P. Pfeiffer, Phys. Rev. D **79**, 024003 (2009).
[61] D. Pollney *et al.*, Phys. Rev. D **76**, 124002 (2007).
[62] G. B. Cook, Phys. Rev. D **65**, 084003 (2002).
[63] J. W. York, Phys. Rev. Lett. **82**, 1350 (1999).
[64] H. P. Pfeiffer and J. W. York, Phys. Rev. D **67**, 044022 (2003).
[65] H. P. Pfeiffer, D. A. Brown, L. E. Kidder, L. Lindblom, G. Lovelace, and M. A. Scheel, Classical Quantum Gravity **24**, S59 (2007).
[66] J. D. Brown and J. W. York, Phys. Rev. D **47**, 1407 (1993).
[67] A. Ashtekar and B. Krishnan, Living Rev. Relativity **7**, 10 (2004).
[68] R. Owen, Ph.D. thesis, California Institute of Technology, 2007, URL http://resolver.caltech.edu/CaltechETD:etd-05252007-143511.
[69] O. Dreyer, B. Krishnan, D. Shoemaker, and E. Schnetter, Phys. Rev. D **67**, 024018 (2003).
[70] G. B. Cook and B. F. Whiting, Phys. Rev. D **76**, 041501 (2007).
[71] L. Lindblom, M. A. Scheel, L. E. Kidder, R. Owen, and O. Rinne, Classical Quantum Gravity **23**, S447 (2006).
[72] H. Friedrich, Commun. Math. Phys. **100**, 525 (1985).
[73] D. Garfinkle, Phys. Rev. D **65**, 044029 (2002).
[74] F. Pretorius, Classical Quantum Gravity **22**, 425 (2005).
[75] C. Gundlach, J. M. Martin-Garcia, G. Calabrese, and I. Hinder, Classical Quantum Gravity **22**, 3767 (2005).
[76] O. Rinne, Classical Quantum Gravity **23**, 6275 (2006).
[77] O. Rinne, L. Lindblom, and M. A. Scheel, Classical Quantum Gravity **24**, 4053 (2007).
[78] J. M. Stewart, Classical Quantum Gravity **15**, 2865 (1998).
[79] H. Friedrich and G. Nagy, Commun. Math. Phys. **201**, 619 (1999).
[80] J. M. Bardeen and L. T. Buchman, Phys. Rev. D **65**, 064037 (2002).
[81] B. Szilágyi, B. Schmidt, and J. Winicour, Phys. Rev. D **65**, 064015 (2002).
[82] G. Calabrese, J. Pullin, O. Reula, O. Sarbach, and M. Tiglio, Commun. Math. Phys. **240**, 377 (2003).
[83] B. Szilágyi and J. Winicour, Phys. Rev. D **68**, 041501(R) (2003).
[84] L. E. Kidder, L. Lindblom, M. A. Scheel, L. T. Buchman, and H. P. Pfeiffer, Phys. Rev. D **71**, 064020 (2005).
[85] L. T. Buchman and O. C. A. Sarbach, Classical Quantum Gravity **23**, 6709 (2006).
[86] L. T. Buchman and O. C. A. Sarbach, Classical Quantum Gravity **24**, S307 (2007).
[87] D. Gottlieb and J. S. Hesthaven, J. Comput. Appl. Math. **128**, 83 (2001).
[88] J. S. Hesthaven, Applied Numerical Mathematics **33**, 23 (2000).
[89] M. A. Scheel, H. P. Pfeiffer, L. Lindblom, L. E. Kidder, O. Rinne, and S. A. Teukolsky, Phys. Rev. D **74**, 104006 (2006).
[90] M. Boyle and A. H. Mroué, arXiv:0905.3177.
[91] B. Brügmann, J. A. González, M. Hannam, S. Husa, U. Sperhake, and W. Tichy, Phys. Rev. D **77**, 024027 (2008).
[92] L. Lindblom and B. Szilágyi, Phys. Rev. D **80**, 084019 (2009).
[93] B. Szilagyi, L. Lindblom, and M. A. Scheel, Phys. Rev. D **80**, 124010 (2009).
[94] E. Poisson, Phys. Rev. D **70**, 084044 (2004).
[95] E. Poisson and I. Vlasov, arXiv:gr-qc/0910.4311v1.
[96] N. Yunes and J. Gonzalez, Phys. Rev. D **73**, 024010 (2006).
[97] A. Buonanno, L. E. Kidder, and L. Lehner, Phys. Rev. D **77**, 026004 (2008).
[98] E. Barausse and L. Rezzolla, Astrophys. J. **704**, L40 (2009).
[99] M. Kesden, Phys. Rev. D **78**, 084030 (2008).
[100] W. Tichy and P. Marronetti, Phys. Rev. D **78**, 081501 (2008).
[101] L. Boyle and M. Kesden, Phys. Rev. D **78**, 024017 (2008).